Strain as a global factor in stabilizing the ferroelectric properties of ZrO 2

Xu, B., Lomenzo, P. D., Kersch, A., Schenk, T., Richter, C., Fancher, C. M., Starschich, S., Berg, F., Reinig, P., Holsgrove, K. M., Kiguchi, T., Mikolajick, T., Boettger, U., & Schroeder, U. (2023). Strain as a global factor in stabilizing the ferroelectric properties of ZrO 2. *Advanced Functional Materials*. Advance online publication. https://doi.org/10.1002/adfm.202311825

Published in:
Advanced Functional Materials

Document Version:
Publisher's PDF, also known as Version of record

ADVANCED FUNCTIONAL MATERIALS
www.afm-journal.de

Strain as a Global Factor in Stabilizing the Ferroelectric Properties of ZrO_2

Bohan Xu, Patrick D. Lomenzo, Alfred Kersch, Tony Schenk, Claudia Richter, Chris M. Fancher, Sergej Starschich, Fenja Berg, Peter Reinig, Kristina M. Holsgrove, Takanori Kiguchi, Thomas Mikolajick, Ulrich Boettger, and Uwe Schroeder**

Since the discovery of ferroelectricity in doped HfO_2 and ZrO_2 thin films over a decade ago, fluorite-structured ferroelectric thin films have attracted much research attention due to their excellent scalability and complementary metal-oxide semiconductor compatibility compared to conventional perovskite ferroelectric materials. Although various factors influencing the formation of the ferroelectric properties are identified, a clear understanding of the causes of the phase formation have been difficult to determine. In this work, ZrO_2 films deposited by atomic layer deposition and chemical solution deposition have resulted in films with completely different structural properties. Regardless of these differences, a general relationship between strain and phase formation is established, leading to a more unified understanding of ferroelectric phase formation in undoped ZrO_2 films, which can be applied to other fluorite-structured films.

1. Introduction

Fluorite-structured ferroelectrics have attracted much attention since ferroelectricity was reported in 10 nm thin polycrystalline films of Si:HfO_2 prepared by atomic layer deposition (ALD).[1] The development of HfO_2-based ferroelectric memory devices drove much of the initial research efforts.[2–4] Since the original publication, the spectrum of prospective applications has quickly widened, and the fluorite-structured films are now also viewed as a promising candidate for use in supercapacitors,[5,6] tunable microwave filters and phase shifters,[7,8] as well as piezoelectric and pyroelectric devices,[9–12] extending research efforts toward actuators, sensors, and resonators. One advantage compared to conventional perovskite ferroelectrics is that these materials are based on simple binary oxides such as HfO_2 and ZrO_2, and are compatible with complementary metal–oxide–semiconductor processes.[1,13]

In the polycrystalline fluorite-structured thin films, a non-centrosymmetric orthorhombic phase with a space group of $Pca2_1$ introduces the ferroelectric behavior.[1,13–15] However, the presence of some other non-ferroelectric phases has been reported as well, including the non-polar $P2_1/c$ monoclinic and

B. Xu, P. D. Lomenzo, T. Schenk, C. Richter, T. Mikolajick, U. Schroeder
NaMLab gGmbH
Noethnitzer Str. 64 a, 01187 Dresden, Germany
E-mail: Bohan.Xu@namlab.com; Uwe.Schroeder@namlab.com
A. Kersch
Munich University of Applied Sciences
80335 Munich, Germany
T. Schenk
Ferroelectric Memory Company
01099 Dresden, Germany
C. M. Fancher
Neutron Scattering Science Directorate
Oak Ridge National Laboratory
Oak Ridge, TN 37831, USA
The ORCID identification number(s) for the author(s) of this article can be found under https://doi.org/10.1002/adfm.202311825

DOI: 10.1002/adfm.202311825

S. Starschich, F. Berg
Institut für Werkstoffe der Elektrotechnik 2
RWTH Aachen University
Sommerfeldstraße 24, 52074 Aachen, Germany
P. Reinig, U. Boettger
Fraunhofer Institut für Photonische Mikrosysteme IPMS (CNT)
An der Bartlake 5, 01109 Dresden, Germany
K. M. Holsgrove
School of Mathematics and Physics
Queen's University Belfast
Belfast, Northern Ireland BT7 1NN, UK
T. Kiguchi
Tohoku University
2-1-1 Katahira, Aoba-ku, Sendai, Miyagi 980–8577, Japan
T. Kiguchi
Kumamoto University
2-39-1 Kurokami, Chuo-ku, Kumamoto 860–8555, Japan
T. Mikolajick
TU Dresden
Noethnitzer Str. 64, 01187 Dresden, Germany

$P4_2/nmc$ tetragonal phases,[13,16] as well as the antipolar *Pbca* orthorhombic phase.[17,18] Therefore, stabilizing the polar o-phase is critical for achieving the functionalities based on the ferroelectric properties.

ZrO_2, as a fluorite-structured material, has been commonly reported as a non-ferroelectric material because the non-polar t-phase is typically the most stable phase in ZrO_2 films,[13,15] and antiferroelectric-like (AFE-like) hysteresis loops have been normally observed, which are caused by a reversible electric field induced t- to o-phase transition.[13,19] Recently, however, ferroelectric properties of undoped ZrO_2 have been reported.[20–25] It is worth noting that a ferroelectric *R3m* rhombohedral phase has been reported in epitaxial ZrO_2 films.[25] Compared to the HfO_2-based thin films, ZrO_2 films can exhibit ferroelectric behavior in a wide thickness range, from subnanometer to 390 nm,[20,26] where the polar o-phase is suppressed in undoped HfO_2 films due to the m-phase formation. In addition, the lower crystallization temperature of thin ALD ZrO_2 films results in better back-end of line compatibility.

The relationship between ferroelectric behavior and strain/stress has recently received increasing attention.[27–31] The strain and stress can be influenced by lattice mismatch,[32] coefficient of thermal expansion (CTE) difference between the film and substrate,[33,34] grain size and surface energy,[15,35] defect content,[36,37] and densification during crystallization.[1,35] Density functional theory (DFT) suggests that large in-plane biaxial compressive stress may stabilize the polar phase and t-phase over the m-phase thermodynamically.[15,38] The suggestion from the point of view of the kinetic barrier is different. DFT suggests a lower barrier for biaxial tensile stress for both t-phase to o-phase and t-phase to m-phase transitions.[39]

Chemical solution deposition (CSD) is an alternative to ALD for depositing fluorite-structured thin films. In CSD-prepared films, the ferroelectric behavior can be observed in ZrO_2 films up to the thickness of 390 nm and in La:HfO_2 even up to 1 μm.[20,40] However, ALD films exhibit a drastic reduction in the ferroelectric properties as the film thickness increases beyond 50 nm, with the polar o-phase destabilization and the non-polar m-phase formation.[41]

In this work, ALD and CSD deposited ZrO_2 in a wide thickness range are used as a model system to understand the ferroelectric stabilization mechanism in thick CSD films, as well as the impact of strain on the ferroelectric properties for both CSD and ALD films. Here, different changes in strain with thickness are expected. Based on this, a model of the relationship between the ferroelectric o-phase stabilization and biaxial strain is developed for different fluorite-structured films, especially for ZrO_2-based thin films.

2. Results and Discussion

2.1. Structural Analysis in the Pristine State

Since the ferroelectric properties in ZrO_2 thin films are highly related to the structural polymorphism, the phase fractions in the pristine state of the films with different thicknesses for both ALD and CSD films are characterized by using grazing incidence x-ray diffractometry (GIXRD), Raman spectroscopy, and transmission electron microscopy (TEM).

According to the GIXRD measurements (**Figure 1**a,b), generally, for both ALD and CSD ZrO_2 films, the o-/t-phases are the phases with the highest peak intensity at 2θ of 30.4°, and the m-phase fraction increases in the thicker films. For ALD films, the m-phase appears in films thicker than 15 nm, and it becomes pronounced when the thickness reaches 45 nm, especially for $(-111)_m$ plane at 2θ of 28.5°. In contrast, the CSD films exhibit a relatively lower m-phase content, even when the films are considerably thicker than the 45 nm thick ALD film. Additionally, it is worth noting that the shoulder peak at 2θ of 31° is not attributed to either the m-phase or the t-phase.[27]

Since the amount of the t- and o-phases cannot be clearly distinguished by GIXRD due to the similarity of the diffraction patterns, Raman spectroscopy has recently been proposed to give a relatively clearer distinction between the o- and t-phase.[42,43] Due to the similarities between polar and antipolar o-phases in the Raman spectra, the o-phases are difficult to distinguish.[44] Raman spectra are measured directly on the ZrO_2 bare surface between the top electrodes for ALD and CSD films with different thicknesses (Figure 1c,d). However, the Raman intensity in films thinner than 30 nm is too weak for good signals, so spectra are only available for 30 and 45 nm thick ALD ZrO_2 films. Similar behavior is observed for both ALD and CSD films with different thicknesses. The m- and t-phases are the most noticeable phases, and the peak intensity for the m-phase increases, which is consistent with the GIXRD results, and the t-phase intensity decreases in thicker ZrO_2 films.

Since the o-phases are almost invisible for both ALD and CSD ZrO_2 films in the Raman spectra, high-resolution TEM (HRTEM) is applied to 45 nm thick ALD ZrO_2 film (**Figure 2**a), and high-angle annular dark-field scanning transmission electron microscopy (HAADF-STEM) is applied to 66 nm thick CSD ZrO_2 film (Figure 2b), respectively. For both films, it is confirmed that the t-phase is the dominant phase, with small amounts of the o-phase, based on the positions of the zirconium atoms monitored by TEM. Overall, the fraction of the o-phase appears very limited in both films, and the o-phase grains are rarely observed across the film in TEM. This explains why the o-phase is not detected by Raman spectroscopy. Furthermore, it is hard to detect the oxygen atoms with HRTEM for distinguishing the antipolar (*Pbca*) and polar ($Pbc2_1$) o-phases.[17,18]

In summary, from the structural analysis in the pristine state of the films, it is observed that the m-, o-, and t-phases coexist in both ALD and CSD films. In the pristine state of the films, the t-phase is the dominant phase, while the o-phase fraction is very low. The m-phase fraction rises and the t-phase fraction reduces with increasing film thickness. In addition, with increasing thickness, the m-phase is more easily stabilized in the ALD layers than in CSD layers.

2.2. Electrical Characterization

The polarization and current hysteresis loops are measured after 10^4 electrical wake-up cycles for ALD films (**Figure 3**a) and 10 electrical wake-up cycles for CSD films (Figure 3b) with different thicknesses, respectively. For ALD films, the hysteresis loop changes from a pinched double hysteresis AFE-like loop to the

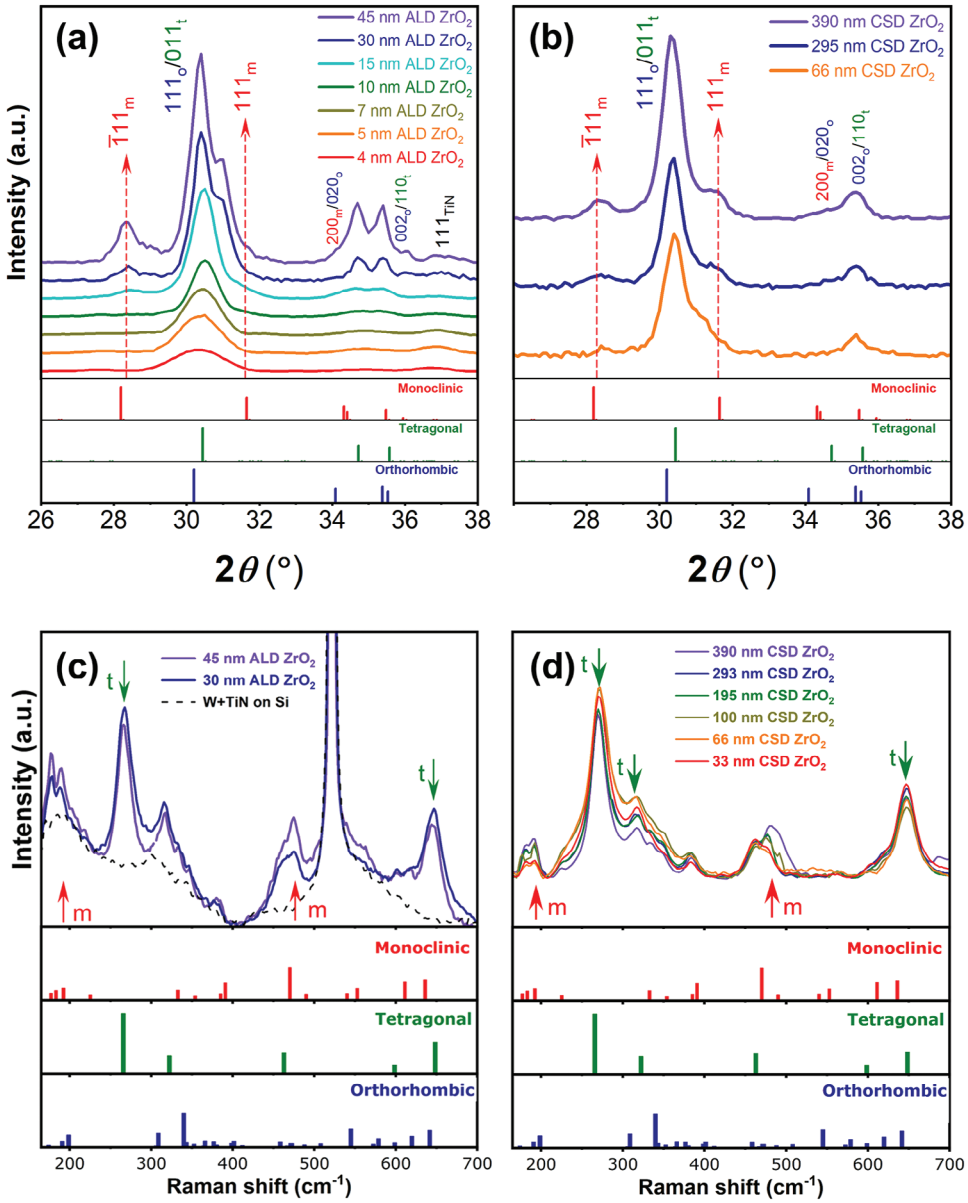

Figure 1. GIXRD measurements for a) ALD ZrO_2 and b) CSD ZrO_2 films with different thicknesses. Raman spectra for c) ALD ZrO_2 and d) CSD ZrO_2 films with different film thicknesses.

ferroelectric hysteresis loop with increasing film thickness. The applied field is reduced from 4 to 2 MV cm^{-1} when the film increased from 10 to 45 nm because the thicker films exhibit higher leakage current and earlier breakdown during cycling under the electric field of 4 MV cm^{-1}. Additionally, the reduction of the background displacement current is caused by the lower relative dielectric constant in the 45 nm film because of the presence of the low-k monoclinic phase. Increasing the film thickness from 10 to 20 nm increases the remanent polarization (P_r) from 7 to 11 μC cm^{-2} (Figure 3c), which is attributed to the t-phase destabilization and polar o-phase formation. However, after further increasing the thickness of the film, the P_r drops to 6 μC cm^{-2}, which is caused by the polar o-phase suppression and m-phase stabilization. Moreover, the significant drop of the breakdown field and relative dielectric constant with thickness is also attributed to the t-phase destabilization and o-/m-phase formation.[15,16,45,46] Compared with the ALD films, the P_r of CSD films decreases from 12 to 7 μC cm^{-2} with the film thickness increasing from 33 to 390 nm. Furthermore, no field-induced t- to o-phase transition or pinched hysteresis loop is observed after ten wake-up cycles in the CSD films.

Since the structural characterizations are performed in the pristine state and the electrical measurements are carried out after wake-up cycling, the electrical behavior during cycling is measured on the 45 nm ALD film (**Figure 4**a) and 66 nm CSD film (Figure 4b) to investigate the wake-up behavior in detail. Ex-situ Raman spectroscopy measurements are performed after the electrical cycling to observe the phase changes during

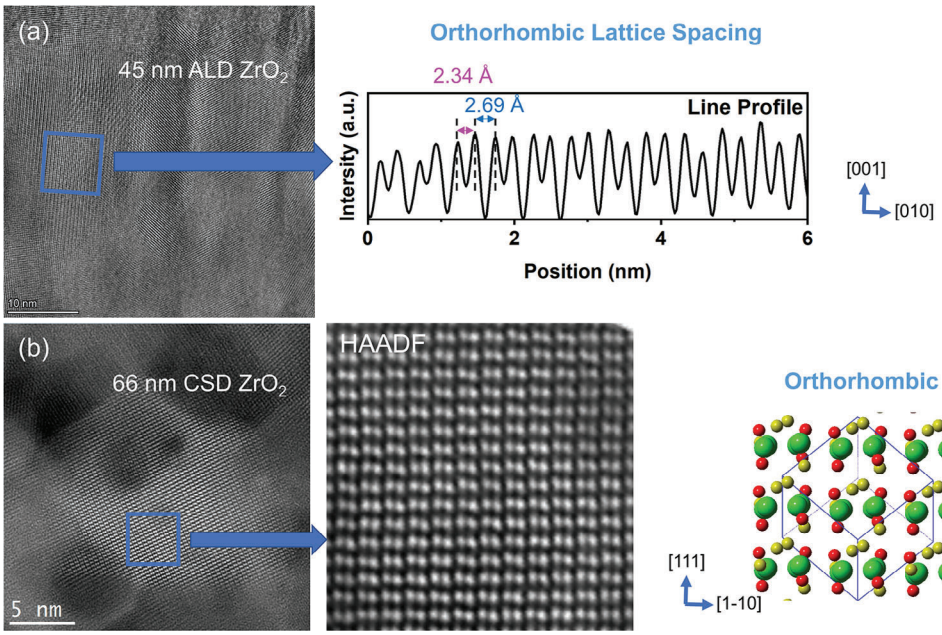

Figure 2. a) Cross-sectional HRTEM measured on 45 nm thick ALD ZrO_2 and b) HAADF-STEM measured on 66 nm thick CSD ZrO_2.

wake-up cycling. For performing the electrical measurements, the top TiN electrodes are sputtered directly on both the ALD and CSD ZrO_2 bare surface due to the limited penetration depth of the Raman laser beam into metals. For ALD films, a wake-up behavior is observed up to 10^4 cycles. Based on Raman spectroscopy (Figure 4d), the t-phase peaks at the Raman shift of 265 and 650 cm^{-1} decrease, and multiple peaks representing the polar o-phase at 340 cm^{-1} and between 550 and 620 cm^{-1} are arising. The antipolar o-phase has the strongest peaks at 355, 560, and 640 cm^{-1}.[44] The increase in the peak intensities can be better correlated with the polar o-phase. However, due to the noise level, the antipolar o-phase cannot be excluded entirely in the pristine and woken-up samples. Since the Raman o-phase intensity increase occurred in parallel with the P_r improvement, the wake-up effect is attributed to the irreversible t- to polar o-phase transition. However, a minor antipolar o-phase contribution could be present. For CSD films, a pinched hysteresis loop in the pristine state indicates the reversible field-induced t- to o-phase transition, and the double switching peaks merge to a single ferroelectric switching peak within 10 electrical cycles. The initial jump to a P_r value of 12 μC cm^{-2} occurs already after the first switching cycle. However, a degradation of the ferroelectric switching peak (fatigue effect) starts after 10 field cycles, and the capacitors start to break down after 10^4 cycles.

In summary, combining the structural and electrical characterizations, a small window for stabilizing the ferroelectric o-phase is observed in ALD films with different thicknesses. The t-phase is stabilized in the thinner films, and the m-phase is formed in the thicker films, both leading to a degradation of the ferroelectric properties, even though the irreversible t- to o-phase transition during cycling improves the ferroelectric behavior. It is worth noting that the t-phase still coexists with the polar o-phase and non-polar m-phase in the 45 nm thick ZrO_2 film after electrical cycling. Compared to the ALD films, CSD films exhibit a larger window of the polar o-phase stabilization with thickness and higher remanent polarization value. More than 70% of the conversion from t-phase to o-phase occurs after the first switching cycle.

2.3. Grain Size and Strain Characterization

As recently discussed, the relationship between the strain/stress and ferroelectric properties in fluorite-structured thin films is an important issue.[27–30,47] Therefore, the biaxial strain and grain size, which plays an essential role in the crystallite surface energy, are characterized and discussed in this section.[15,48]

The grain size is measured on the top surface of the ALD ZrO_2 films and in cross-sections for the CSD ZrO_2 layers. Atomic force microscopy (AFM) in tapping mode is applied to the ALD ZrO_2 films, and scanning electron microscopy (SEM) is used for CSD ZrO_2, respectively. The images are further analyzed with the Gwydion software by applying the watershed method (**Figure 5**a).[49] For ALD films, the grain size increases rapidly up to 20 for 30 nm thick films and remains relatively constant as the film thickness further increases. For CSD films, the grain size is relatively stable at 5 to 10 nm up to a thickness of 390 nm, and the overall grain size is smaller than the grain size in ALD films. Cross-sectional HRTEM is performed on 15 nm ALD ZrO_2 (Figure 5c), 45 nm ALD ZrO_2 (Figure 5d), and 66 nm CSD ZrO_2 (Figure 5e), respectively. For 15 nm ALD ZrO_2, grains span the whole film thickness perpendicular to the substrate, meaning the film thickness restricts the grain size in the thin ALD ZrO_2 films. However, stacking of multiple grains perpendicular to the surface is observed in the 45 nm ALD ZrO_2, indicating that the film thickness in the thicker ALD films no longer restricts the grain size. Additionally, a porous structure is shown in the CSD ZrO_2 films,

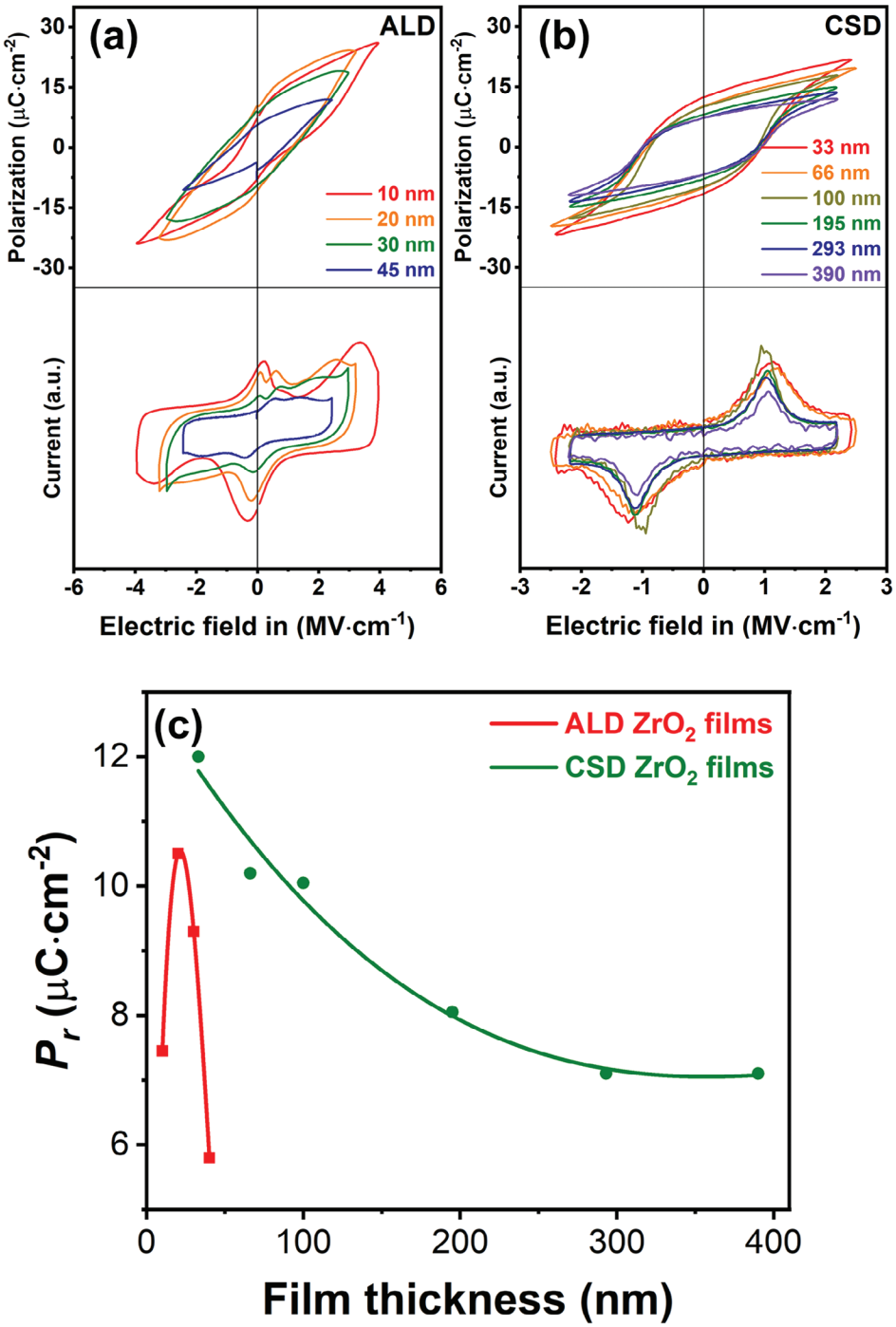

Figure 3. Polarization (top) and current (bottom) hysteresis loops for (a) ALD films after 10^4 wake-up cycles and (b) CSD films after 10 wake-up cycles with different film thicknesses. c) The extracted remanent polarization as a function of film thickness for both ALD and CSD films.

which is likely from the outgassing of residual solvents. The grain size is thereby limited by the pores during the homogeneous nucleation instead of the film thickness.[40] Interestingly, a similar porous structure formed during the process has been reported in ferroelectric CeO_2-HfO_2 solid solution epitaxial thin films.[50,51]

Bragg-Brentano X-ray diffractometry (BBXRD) measurements are carried out with $\sin^2\Psi$ method to extract the lattice spacing changes from out-of-plane ($\Psi = 0$ °) to in-plane ($\Psi = 90$ °) direction for both ALD (**Figure 6**a) and CSD (Figure 6b) films with different thicknesses.[29] The in-plane biaxial strains are calculated based on the lattice spacing changes with a Poisson ratio of 0.29,

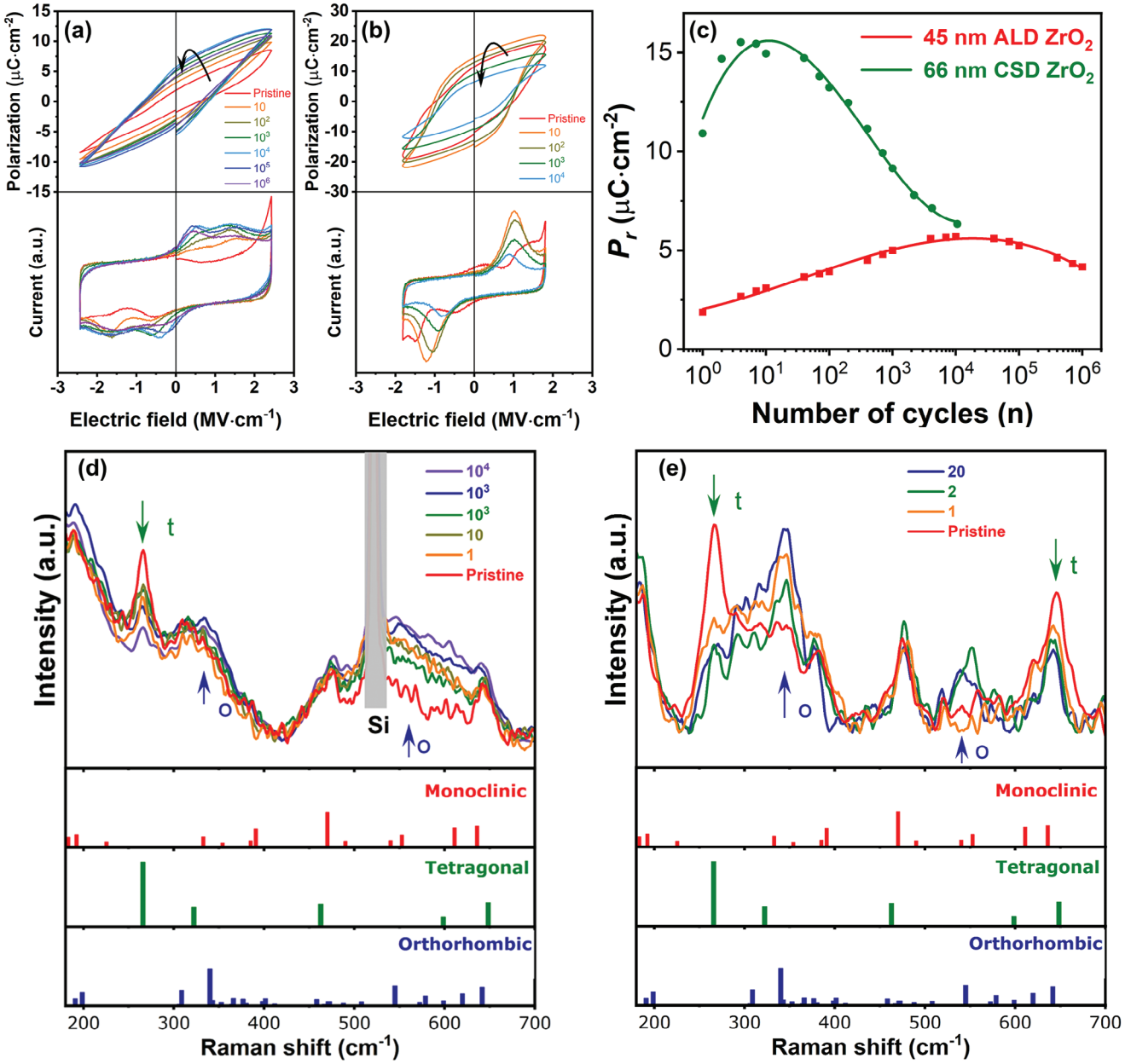

Figure 4. Polarization (top) and current (bottom) hysteresis loops with field cycling for a) a 45 nm thick ALD film and b) a 66 nm thick CSD film. c) Extracted remanent polarization as a function of the number of electric field cycles for both ALD and CSD films. Raman spectroscopy with field cycling for d) 45 nm thick ALD film and e) 66 nm thick CSD film.

and the stresses are determined assuming a Young's modulus of 267 GPa.[52] More details are discussed in the Supporting Information (Figure S1, Supporting Information). For both ALD and CSD films, the in-plane tensile strain and stress decrease in the thicker films. However, the values decrease much faster in ALD films compared to CSD films (Figure 6c).

As discussed, many factors influence the strain in the ZrO_2 films, including lattice mismatch and CTE difference between the film and substrate,[32–34] phase stabilization,[53] defect content,[36,37] and densification during annealing,[1,35] etc. These factors can also be interrelated. The lattice mismatch between the film and substrate is also influenced by film thickness because the lattice mismatch is larger at the interface than in the bulk. Therefore, in thicker films, the bulk is more critical than the interface in terms of strain reduction. However, it cannot fully explain that the strain decreases much faster in the ALD films, especially since the lattice parameter of the TiN electrode (≈4.1 Å), which is used in ALD films, is closer to the ZrO_2 (≈5 Å) compared to the lattice parameter of the Pt electrode (≈3.9 Å), which is used in CSD films. Film growth is a major factor influencing the strain in the film. During film deposition, grain formation and grain growth reduce the strain in the film with increasing thickness.[54] The other factor is phase stabilization. Since the volumes of the m-, o-, and t-phases follow the order of $V_m > V_o > V_t$,[15] the film

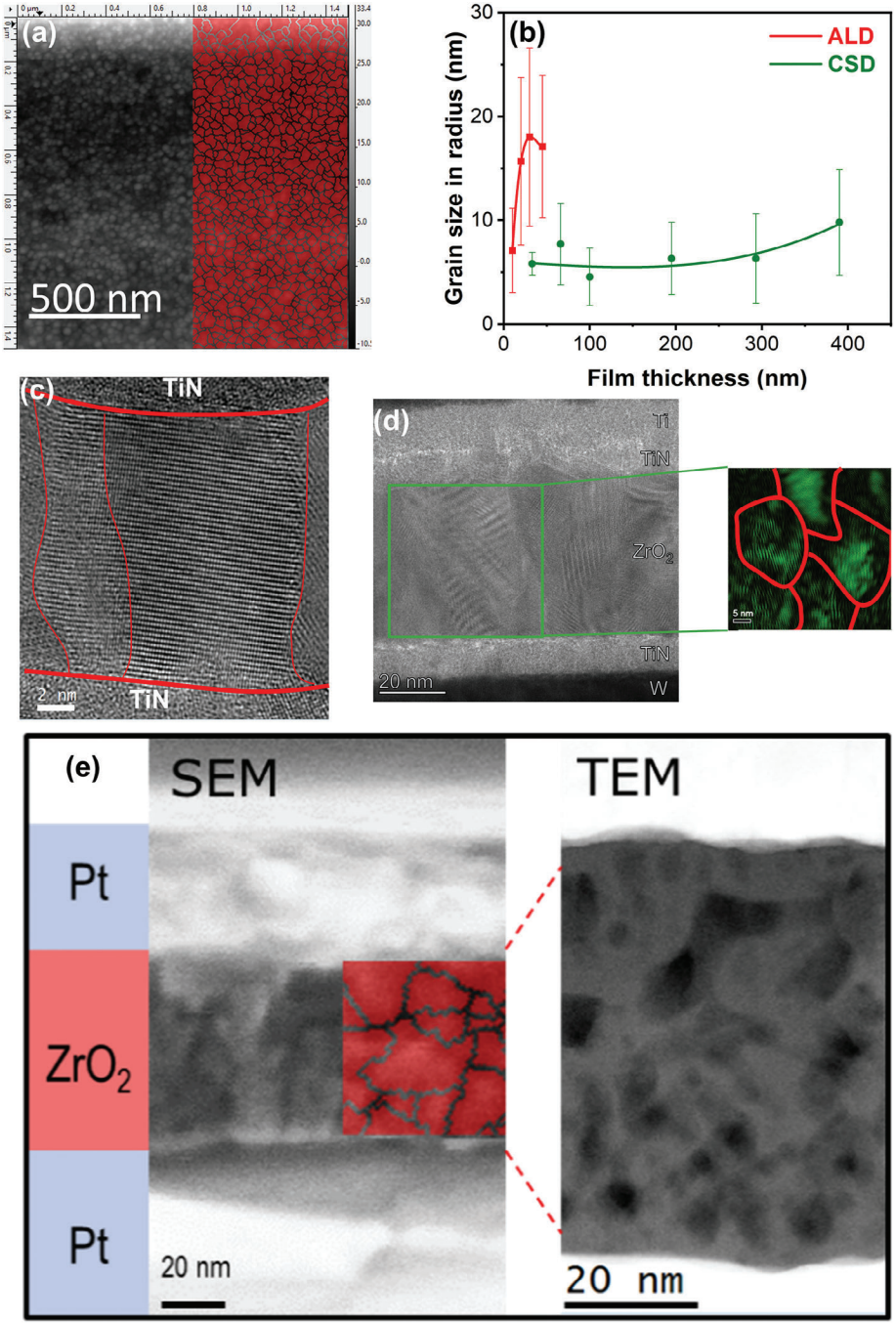

Figure 5. a) AFM scan of the top surface of a 45 nm thick ALD ZrO_2. The region in red shows the analysis by the watershed method with Gwydion. b) Gain radius as a function of film thickness for both ALD and CSD ZrO_2 films. c) Cross-sectional HRTEM image of a 15 nm thick ALD ZrO_2 film. d) Cross-sectional HRTEM image of a 45 nm thick ALD ZrO_2 as well as the inverse fast Fourier transform (masking $\{111\}_o/\{011\}_t$ planes) of the area marked by the green square. Grains are outlined in red. e) Cross-sectional SEM and HAADF-STEM images of a 66 nm CSD ZrO_2 film.

stabilized in the m-phase exhibits the smallest in-plane tensile strain in the film, and the film stabilized in the t-phase shows the largest strain.[53] Therefore, the in-plane strain in the ALD films drops faster in the thicker films since the m-phase is easier stabilized in the ALD films, according to the structural characterization in the pristine state of the film. In contrast, the prominent surface-to-volume ratio generated from the porosity in the CSD films suppresses the m-phase formation, giving a larger window for the polar o-phase stabilization with thickness. Furthermore, even though the t-phase is energetically favorable due to the large surface-to-volume ratio in the pristine state of the CSD films,[15] the porosity also eases the irreversible t- to o-phase transition during electrical cycling, leading to a decent ferroelectric behavior after wake-up cycling.

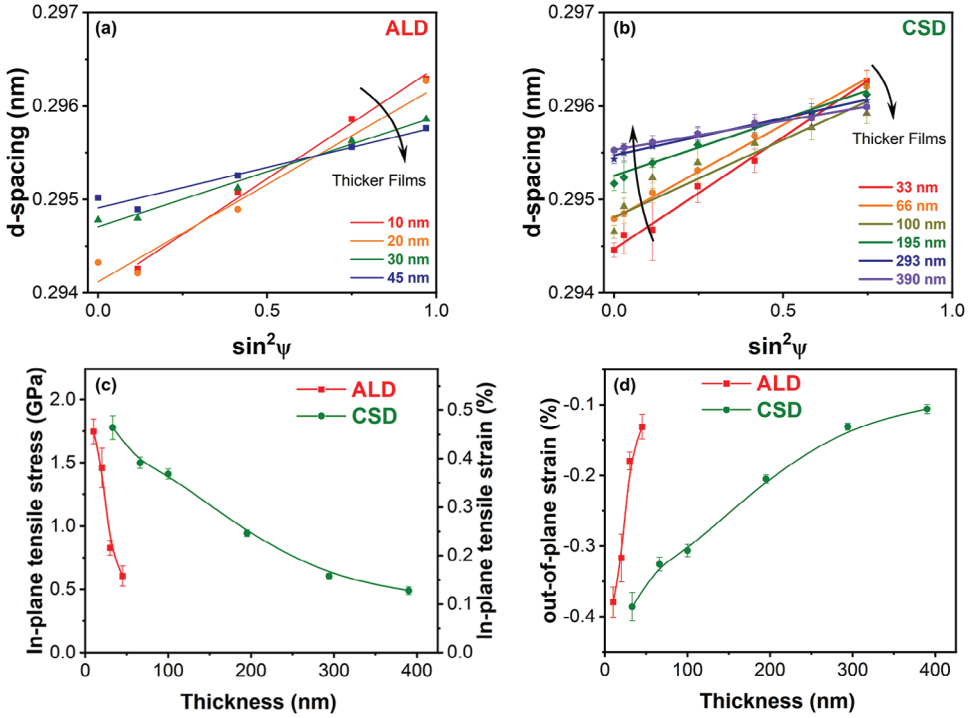

Figure 6. $Sin^2\Psi$ analysis of the angular dependent BBXRD data for a) ALD and b) CSD ZrO_2 films with various film thicknesses. c) In-plane tensile stress and strain as a function of film thickness and d) corresponding out-of-plane compressive strain as a function of film thickness for both ALD and CSD films.

For further understanding the relationship between the strain and ferroelectric behavior in the ZrO_2 thin films, the in-plane strain as a function of the t- to o-phase transition field or coercive field (E_c) in the pristine sample is shown in **Figure 7**. Since the strain determined by the $sin^2\Psi$ method is measured in the pristine state of the films, the switching field values are also obtained in the pristine state for a fair comparison, as they may be influenced during wake-up field cycling.[55] For the o-phase, the E_c is used as the switching field; for the t-phase, the t- to o-phase transition field is chosen to represent the ferroelectric properties. A larger field required for the t- to o-phase transition illustrates greater t-phase stabilization. These parameters are less influenced by leakage current compared to extracted P_r values (Figure S3, Supporting Information).

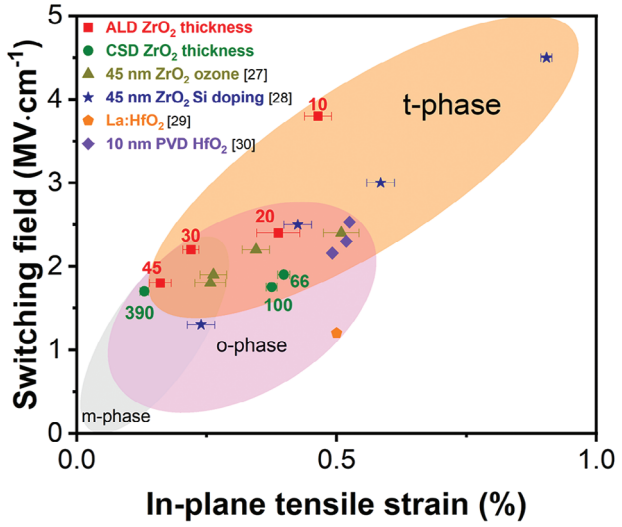

Figure 7. Switching field (E_c for ferroelectric films and t- to o-phase transition field for anti-ferroelectric films) as a function of in-plane-tensile strain for films from different sources. The thicknesses of the ALD films (red) and CSD films (green) from this study are marked next to the data points.

As discussed, the biaxial in-plane tensile strain decreases in thicker films for both ALD and CSD films, revealing the t-phase destabilization with higher film thickness. Moreover, for 30–45 nm ALD, and 390 nm CSD films, an increasing amount of the non-polar m-phase, consistent with a decrease of the in-plane tensile strain, is observed from GIXRD.

Additional data from other references were added, and a common trend is shown (Figure 7). All factors, such as film compositions, deposition methods, annealing conditions, doping, oxygen vacancy content, surface energy, etc. are different in those films, leading to a specific strain in the layer that correlates with the phase. As a result, a consistent trend is observed for these films. A high strain corresponds to forming a t-phase with a high transition field from t- to o-phase. Reducing the strain would reduce the field for the phase transition until the coercive field of the o-phase is reached. For strain values below 0.3%, the m-phase is favored. The trend appears to be universal, as both ALD and CSD films follow the same tendency in addition to other samples. Overall, it should be noted that non-polar interfacial layers between the electrode and the dielectric results in a depolarization field that

increases the switching field. This effect is more critical for thinner films and causes a broadening of the general strain versus switching field trend.[56]

3. Conclusion

This paper compares and discusses undoped ZrO_2 films deposited by ALD and CSD with different thicknesses. Many factors are different for ALD and CSD films, including film thickness, deposition temperature, electrode material, annealing conditions, oxygen and defect concentration in ZrO_2, etc. As a result, ALD films have a polycrystalline granular and CSD films have a porous structure. However, the stabilization of phases is still found to be similar. Here, a global commonality for these films is observed in the sense that a large in-plane tensile strain stabilizes the t-phase, a small in-plane tensile strain favors the m-phase, and the ferroelectric o-phase is stabilized with an intermediate strain. This also seems much more generally true for all doped HfO_2 and mixed HZO films with fluorite structure. As the main difference between both deposition methods, it is found that the larger in-plane tensile strain and surface-to-volume ratio in CSD films introduce a larger window in thicknesses for ferroelectric stabilization.

Currently, compatibility and reliability are widely studied for the use of fluorite-structured thin films for memory and other applications. By understanding the relationship between strain and ferroelectric properties in fluorite-structured films, various process parameters can be changed simultaneously during film development if strain conditions are kept constant.

4. Experimental Section

Capacitor Fabrication: For CSD films, capacitors of undoped ZrO_2 films with thicknesses ranging from 33 and 390 nm were prepared by CSD. Zirconium 2,4-pentadionate was dissolved in propionic acid and propionic acid anhydrite (5:3) at 140 °C for 6 h as the precursor solution. The prepared precursor solution with a concentration of 0.25 mol L^{-1} was spin-coated on a sputtered 100 nm platinum (Pt) bottom electrode with a (111) orientation. After each spinning coating, a heating step was performed at 215 °C for 5 min. The spin coating process was repeated several times to achieve the desired film thickness. A final crystallization step was carried out at 800 °C for 90 s in an oxygen/argon atmosphere (1:1). A 50 nm thick Pt top electrode was sputtered at room temperature, and a negative lift-off process was performed to structure the Pt top electrode. For ALD films, capacitors of undoped ZrO_2 films with thicknesses from 4 to 45 nm were prepared by ALD. 30 nm thick tungsten (W) conducting layer and 10 nm thick titanium nitride (TiN) bottom electrode were subsequently sputtered at room temperature. C_p-$Zr[N(CH_3)_2]_3$ was used as a metal-organic precursor to deposit ZrO_2 films with different thicknesses at 350 °C with an oxidizer of ozone. A 10 nm TiN top electrode was then sputtered on the ZrO_2 films. 10 nm titanium (Ti) and 25 nm Pt hard mask dots were evaporated through a shadow mask. The bare TiN top electrode was etched with inductively coupled plasma (ICP) to complete the top electrode structure. No additional annealing step was required for crystallization.

X-Ray Diffraction: Grazing incidence X-ray diffractometry and Bragg-Brentano X-ray diffractometry measurements were performed in a Bruker D8 Discover tool with 0.154 nm Cu-K_α radiation.

Raman Spectroscopy: A Renishaw inVia Qontor Raman microscope was used for ALD films to conduct Raman measurements with an exposure time of 5000 s per spectrum. A Leica DM2700 microscope (×100) with an argon laser of a 457 nm wavelength was used in Raman. For CSD films, Raman spectroscopy was performed at room temperature using a confocal Raman microscope (inVia Qontor, Renishaw plc), including a DM2700 microscope (Leica Camera AG) and 100× NPLAN-objective lens. For excitation, a solid-state continuous wave (cw) laser (TEM_{00}, polarization ratio 100:1, vertical) operating at (405,0 ± 0,5) nm wavelength with a maximum output power of 30 mW has been employed. Sample illumination was performed perpendicular to the sample surface. Measurements were conducted in the Stokes-regime using a Rayleigh filter with 100 cm^{-1} cut-off wavenumbers. Raman spectra acquisition was conducted at an exposure time of 1200 s per individual spectrum and integration of three subsequent individual measurements. A baseline correction was performed after measuring the raw spectra for both ALD and CSD films.

Atomic Force Microscopy: A Bruker Dimension XR scanning probe microscope was utilized to characterize the surface roughness and grain size on the surface.

Scanning Electron Microscopy: Cross-sectional and top-view images were obtained by scanning electron microscopy using a Zeiss Leo 1560 equipped with a field-emission cathode.

Transmission Electron Microscopy: Cross-sectional specimens for electron microscopy were prepared using a Tescan-focused ion beam (FIB)—secondary electron microscope Lyra 3. FIB milling was performed at accelerating voltages of 30 and 5 kV. High-resolution transmission electron microscopy was performed on a Thermo Fisher Scientific Talos F200X and JEOL JEM-ARM200F operated at 200 kV.

Electrical Characterization: The CSD films with the top electrode area of approximately 2500 μm^2 were measured using an AixACCT TF 2000 ferroelectric analyzer with a frequency of 1 kHz. The ALD films with the top electrode area of approximately 9500 μm^2 were measured using an AixACCT TF 3000 ferroelectric analyzer with a frequency of 1 kHz.

Density Functional Theory: First principles calculations were performed using the ABINIT implementation of the density functional theory and the density functional perturbation theory (DFPT) using the Local Density Approximation (LDA) and Projector Augmented Wave (PAW) pseudopotentials from the GBRV library. The plane wave cut-off was 40 Ha and the PAW cut-off 45 Ha. For the 6-atomic $P4_2/nmc$ t-phase, the reciprocal space was sampled with a mesh of size $8 \times 8 \times 6$. The force criterion for the atomic relaxation was better than 10^{-4} eV $Å^{-1}$ and the structures were fully relaxed. Phonons were calculated at the Gamma-point. The Raman tensor was calculated using third-order DFPT. Biaxial stress was applied in the *xy* and *xz*-plane (equal to *yz*-plane) to calculate the stress dependence of the Raman frequencies, resulting in frequency shifts. Assuming isotropic orientation of the grains, the average shift was computed as an average of 1 weight *xy*-shift and 2 weights *xz*-shift.

Supporting Information

Supporting Information is available from the Wiley Online Library or from the author.

Acknowledgements

B.X. and P.D.L. were financially supported by the Deutsche Forschungs Gemeinschaft (DFG) within the following projects (Zeppelin (433647091) and Homer (430054035)). The work of P.R. was partly funded by the Federal Ministry of Education and Research (BMBF) under the project reference numbers 16FMD01K, 16FMD02 and 16FMD03. S.S., F.B., and U.B. were financially supported by the DFG with the project Zeppelin (433647091). T.S. and C.R. were financed by DFG "Inferox" project (MI 1247/11-2). T.M. and U.S. were financially supported out of the Saxonian State budget approved by the delegates of the Saxon State Parliament. This work was co-financed from the tax revenues on the basis of the budget adopted by the Saxon State Parliament.

Open access funding enabled and organized by Projekt DEAL.

Conflict of Interest

The authors declare no conflict of interest.

Data Availability Statement

The data that support the findings of this study are available from the corresponding author upon reasonable request.

Keywords

ferroelectricity, strain, stress, thin film, zirconia

Received: September 26, 2023
Revised: October 23, 2023
Published online:

[1] T. S. Böscke, J. Müller, D. Bräuhaus, U. Schröder, U. Böttger, *Appl. Phys. Lett.* **2011**, *99*, 102903.
[2] J. Müller, T. S. Böscke, S. Müller, E. Yurchuk, P. Polakowski, J. Paul, D. Martin, T. Schenk, K. Khullar, A. Kersch, W. Weinreich, S. Riedel, K. Seidel, A. Kumar, T. M. Arruda, S. V. Kalinin, T. Schlösser, R. Boschke, R. van Bentum, U. Schröder, T. Mikolajick, presented at *Tech Dig Int Electron Devices Meet*, Washington, DC,USA, **2013**, pp 10.8.1–10.8.4.
[3] T. Mikolajick, S. Müller, T. Schenk, E. Yurchuk, S. Slesazeck, U. Schröder, S. Flachowsky, R. van Bentum, S. Kolodinski, P. Polakowski, J. Müller, *Adv. Sci. Technol.* **2014**, *95*, 136.
[4] P. Polakowski, S. Riedel, W. Weinreich, M. Rudolf, J. Sundqvist, K. Seidel, J. Muller, presented at *IEEE 6th International Memory Workshop (IMW)*, Taipei, Taiwan, **2014**, pp. 1-4.
[5] M. H. Park, H. J. Kim, Y. J. Kim, T. Moon, K. D. Kim, C. S. Hwang, *Adv. Energy Mater.* **2014**, *4*, 1400610.
[6] F. Ali, X. Liu, D. Zhou, X. Yang, J. Xu, T. Schenk, J. Müller, U. Schroeder, F. Cao, X. Dong, *J. Appl. Phys.* **2017**, *122*, 144105.
[7] M. Dragoman, M. Modreanu, I. M. Povey, S. Iordanescu, M. Aldrigo, C. Romanitan, D. Vasilache, A. Dinescu, D. Dragoman, *Nanotechnology* **2017**, *28*, 38LT04.
[8] M. Dragoman, M. Aldrigo, M. Modreanu, D. Dragoman, *Appl. Phys. Lett.* **2017**, *110*, 103104.
[9] S. Starschich, U. Böttger, *J. Appl. Phys.* **2018**, *123*, 044101.
[10] P. D. Lomenzo, S. Jachalke, H. Stoecker, E. Mehner, C. Richter, T. Mikolajick, U. Schroeder, *Nano Energy* **2020**, *74*, 104733.
[11] S. Jachalke, E. Mehner, H. Stöcker, J. Hanzig, M. Sonntag, T. Weigel, T. Leisegang, D. C. Meyer, *Appl. Phys. Rev.* **2017**, *4*, 021303.
[12] C. Mart, T. Kämpfe, K. Kühnel, M. Czernohorsky, S. Kolodinski, M. Wiatr, W. Weinreich, L. M. Eng, *APL Mater.* **2021**, *9*, 051120.
[13] J. Müller, T. S. Böscke, U. Schröder, S. Mueller, D. Bräuhaus, U. Böttger, L. Frey, T. Mikolajick, *Nano Lett.* **2012**, *12*, 4318.
[14] E. H. Kisi, C. J. Howard, R. J. Hill, *J. Am. Ceram. Soc.* **1989**, *72*, 1757.
[15] R. Materlik, C. Künneth, A. Kersch, *J. Appl. Phys.* **2015**, *117*, 134109.
[16] M. H. Park, Y. H. Lee, H. J. Kim, T. Schenk, W. Lee, K. D. Kim, F. P. G. Fengler, T. Mikolajick, U. Schroeder, C. S. Hwang, *Nanoscale* **2017**, *9*, 9973.
[17] Y. Cheng, Z. Gao, K. H. Ye, H. W. Park, Y. Zheng, Y. Zheng, J. Gao, M. H. Park, J.-H. Choi, K.-H. Xue, C. S. Hwang, H. Lyu, *Nat. Commun.* **2022**, *13*, 645.
[18] X. Li, H. Zhong, T. Lin, F. Meng, A. Gao, Z. Liu, D. Su, K. Jin, C. Ge, Q. Zhang, L. Gu, *Adv. Mater.* **2023**, *35*, 2207736.
[19] P. D. Lomenzo, L. Collins, R. Ganser, B. Xu, R. Guido, A. Gruverman, A. Kersch, T. Mikolajick, U. Schroeder, *Adv. Funct. Mater.* **2023**, *33*, 2303636.
[20] S. Starschich, T. Schenk, U. Schroeder, U. Boettger, *Appl. Phys. Lett.* **2017**, *110*, 182905.
[21] S.-H. Yi, K.-W. Huang, H.-C. Lin, M.-J. Chen, *J. Mater. Chem. C* **2020**, *8*, 3669.
[22] C.-Y. Wang, C.-I. Wang, S.-H. Yi, T.-J. Chang, C.-Y. Chou, Y. T. Yin, M. Shiojiri, M.-J. Chen, *Mater. Des.* **2020**, *195*, 109020.
[23] K. Chae, S. F. Lombardo, N. Tasneem, M. Tian, H. Kumarasubramanian, J. Hur, W. Chern, S. Yu, C. Richter, P. D. Lomenzo, M. Hoffmann, U. Schroeder, D. Triyoso, S. Consiglio, K. Tapily, R. Clark, G. Leusink, N. Bassiri-Gharb, P. Bandaru, J. Ravichandran, A. Kummel, K. Cho, J. Kacher, A. I. Khan, *ACS Appl. Mater. Interfaces* **2022**, *14*, 36771.
[24] A. P. S. Crema, M. C. Istrate, A. Silva, V. Lenzi, L. Domingues, M. O. Hill, V. S. Teodorescu, C. Ghica, M. J. M. Gomes, M. Pereira, L. Marques, J. L. Macmanus-Driscoll, J. P. B. Silva, *Adv. Sci.* **2023**, *10*, 2207390.
[25] J. P. B. Silva, R. F. Negrea, M. C. Istrate, S. Dutta, H. Aramberri, J. Íñiguez, F. G. Figueiras, C. Ghica, K. C. Sekhar, A. L. Kholkin, *ACS Appl. Mater. Interfaces* **2021**, *13*, 51383.
[26] S. S. Cheema, N. Shanker, S.-L. Hsu, Y. Rho, C.-H. Hsu, V. A. Stoica, Z. Zhang, J. W. Freeland, P. Shafer, C. P. Grigoropoulos, J. Ciston, S. Salahuddin, *Science* **2022**, *376*, 648.
[27] B. Xu, P. D. Lomenzo, A. Kersch, T. Mikolajick, U. Schroeder, *ACS Appl. Electron. Mater.* **2022**, *4*, 3648.
[28] B. Xu, L. Collins, K. M. Holsgrove, T. Mikolajick, U. Schroeder, P. D. Lomenzo, *ACS Appl. Electron. Mater.* **2023**, *5*, 2288.
[29] T. Schenk, C. M. Fancher, M. H. Park, C. Richter, C. Künneth, A. Kersch, J. L. Jones, T. Mikolajick, U. Schroeder, *Adv. Electron. Mater.* **2019**, *5*, 1900303.
[30] T. Mittmann, M. Michailow, P. D. Lomenzo, J. Gärtner, M. Falkowski, A. Kersch, T. Mikolajick, U. Schroeder, *Nanoscale* **2021**, *13*, 912.
[31] Y.-C. Kao, H.-K. Peng, Y.-K. Wang, K.-A. Wu, C.-Y. Wang, Y.-D. Lin, T.-C. Lai, Y.-H. Wu, C.-Y. Lin, S.-W. Hsiao, M.-H. Lee, P.-J. Wu, *ACS Appl. Electron. Mater.* **2022**, *4*, 3897.
[32] S. Estandía, N. Dix, J. Gazquez, I. Fina, J. Lyu, M. F. Chisholm, J. Fontcuberta, F. Sánchez, *ACS Appl. Electron. Mater.* **2019**, *1*, 1449.
[33] Y. Lee, H. W. Jeong, S. H. Kim, K. Yang, M. H. Park, *Mater. Sci. Semicond. Process.* **2023**, *160*, 107411.
[34] Y. Lee, Y. Goh, J. Hwang, D. Das, S. Jeon, *IEEE Trans. Electron Devices* **2021**, *68*, 523.
[35] M. H. Park, Y. H. Lee, T. Mikolajick, U. Schroeder, C. S. Hwang, *Adv. Electron. Mater.* **2019**, *5*, 1800522.
[36] S. S. Fields, S. W. Smith, C. M. Fancher, M. D. Henry, S. L. Wolfley, M. G. Sales, S. T. Jaszewski, M. A. Rodriguez, G. Esteves, P. S. Davids, S. J. Mcdonnell, J. F. Ihlefeld, *Adv. Mater. Interfaces* **2021**, *8*, 2100018.
[37] T. Mittmann, M. Materano, S.-C. Chang, I. Karpov, T. Mikolajick, U. Schroeder, presented at *IEEE Int. Electron Devices Meet. (IEDM)*, **2020**, pp. 18.4.1–18.4.4, https://doi.org/10.1109/IEDM13553.2020.9372097.
[38] R. Batra, T. D. Huan, J. L. Jones, G. Rossetti, R. Ramprasad, *J. Phys. Chem. C* **2017**, *121*, 4139.
[39] L. Azevedo Antunes, R. Ganser, U. Schroeder, T. Mikolajick, A. Kersch, *ACS Adv. Mater. Interfaces, accepted*.
[40] T. Schenk, N. Godard, A. Mahjoub, S. Girod, A. Matavz, V. Bobnar, E. Defay, S. Glinsek, *Phys. Status Solidi RRL* **2020**, *14*, 1900626.
[41] M. H. Park, T. Schenk, S. Starschich, C. M. Fancher, H. J. Kim, U. Böttger, C. S. Hwang, A. Toriumi, X. Tian, U. Schroeder, In Ferroelectricity in Doped Hafnium Oxide: Materials, Properties and Devices, U. Schroeder, C. S. Hwang, H. Funakubo, Eds., Woodhead Publishing, **2019**, pp. 145–172, https://doi.org/10.1016/B978-0-08-102430-0.00011-5.
[42] M. Materano, P. Reinig, A. Kersch, M. Popov, M. Deluca, T. Mikolajick, U. Boettger, U. Schroeder, *Phys. Status Solidi RRL* **2022**, *16*, 2100589.
[43] U. Schroeder, R. Sachdeva, P. D. Lomenzo, B. Xu, M. Materano, T. Mikolajick, A. Kersch, *J. Appl. Phys.* **2022**, *132*, 214104.
[44] A. Kersch, R. Ganser, M. Trien, *Front Nanotechnol* **2022**, *4*, 1026286.

[45] C. Richter, T. Schenk, M. H. Park, F. A. Tscharntke, E. D. Grimley, J. M. Lebeau, C. Zhou, C. M. Fancher, J. L. Jones, T. Mikolajick, U. Schroeder, *Adv. Electron. Mater.* **2017**, *3*, 1700131.
[46] S. K. Kim, C. S. Hwang, *Electrochem. Solid-State Lett.* **2007**, *11*, G9.
[47] R. Han, P. Hong, S. Ning, Q. Xu, M. Bai, J. Zhou, K. Li, F. Liu, F. Shi, F. Luo, Z. Huo, *J. Appl. Phys.* **2023**, *133*, 240702.
[48] P. D. Lomenzo, M. Materano, T. Mittmann, P. Buragohain, A. Gruverman, T. Kiguchi, T. Mikolajick, U. Schroeder, *Adv. Electron. Mater.* **2022**, *8*, 2100556.
[49] P. Klapetek, D. Necas, C. Anderson, *Czech Metrol. Inst.* **2004**, *2007*, 2009.
[50] T. Shiraishi, S. Choi, T. Kiguchi, T. Shimizu, H. Funakubo, T. J. Konno, *Appl. Phys. Lett.* **2019**, *114*, 232902.
[51] T. Shiraishi, T. J. Konno, H. Funakubo, *Appl. Phys. Lett.* **2022**, *120*, 132901.
[52] S. S. Fields, D. H. Olson, S. T. Jaszewski, C. M. Fancher, S. W. Smith, D. A. Dickie, G. Esteves, M. D. Henry, P. S. Davids, P. E. Hopkins, J. F. Ihlefeld, *Appl. Phys. Lett.* **2021**, *118*, 102901.
[53] S. S. Fields, T. Cai, S. T. Jaszewski, A. Salanova, T. Mimura, H. H. Heinrich, M. D. Henry, K. P. Kelley, B. W. Sheldon, J. F. Ihlefeld, *Adv. Electron. Mater.* **2022**, *8*, 2200601.
[54] C. V. Thompson, R. Carel, *J Mech Phys Solids* **1996**, *44*, 657.
[55] S. T. Jaszewski, S. S. Fields, J. F. Ihlefeld, Presented at *ISAF-ISIF-PFM*, Cleveland **2023**.
[56] P. D. Lomenzo, C. Richter, T. Mikolajick, U. Schroeder, *ACS Appl. Electron. Mater.* **2020**, *2*, 1583.